Selective Excitation of Polarization-preserved Chiral Photoluminescence in Single Plasmonic Nanohelicoids

*Han Gao, Pei-Gang Chen, Tsz Wing Lo, Wei Jin, Dangyuan Lei**

H. Gao, Prof. W. Jin

Department of Electrical Engineering

The Hong Kong Polytechnic University

Hong Kong 999077, China

P. G. Chen, T. W. Lo, Dr. D. Y. Lei

Department of Materials Science and Engineering

City University of Hong Kong

Hong Kong 999077, China

E-mail: dangylei@cityu.edu.hk

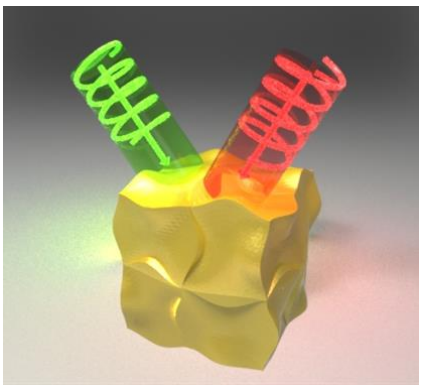

Table of Content: Polarization-preserved chiral photoluminescence can be selectively excited from single plasmonic nanohelicoids with intrinsic chirality.

Abstract

The development of chiral photoluminescence (PL) has drawn extensive attention owing to its potential applications in optical data storage, biosensing and displays. Due to the lack of effective synthesis methods, colloidal metallic nanostructures with intrinsic chiral PL have rarely been reported. Herein, we report for the first time the chiral excitation and emission properties of single gold nanohelicoids (GNHs). By measuring their circular dichroism response and excitation/emission polarization-resolved PL spectra, we reveal that the intrinsic chirality arising from the geometric handedness of the GNHs induces the observed excitation-polarization-correlated chiral PL. Two models are employed to analyze the observed circular-polarization preservation: (1) a chiral PL phenomenological model quantitatively reproduces the PL dissymmetry features; (2) a chiral Purcell effect model reveals that the super-chiral near fields in the GNHs account for the far-field chiral responses such as the polarization-preserved chiral PL. Our findings not only provide important understanding of the physical mechanism responsible for chiral plasmonic nanostructures, but also expand the research on chiral PL-active materials from hybrid achiral/chiral nanostructure systems to metallic nanostructures with intrinsic structural chirality, thereby broadening the scope of applications in three-dimensional chiral imaging and sensing as well as microstructure analysis.

Key words: *chiral photoluminescence, gold nanohelicoids, circular dichroism, structural chirality, chiral Purcell enhancement*

1. Introduction

Photoluminescence (PL) of metal was firstly uncovered experimentally and theoretically by Mooradian in 1969.[1] Later on, colloidal gold nanoparticles (Au NPs) with different shapes including sphere,[2-3] rod,[7] cube, [8] and bipyramid,[9] etc., have been found to exhibit enhanced PL, most of which are attributed to the excitation of localized surface plasmons (LSPs) in the NPs.[3] In recent years, plasmonic system formed by metallic nanoparticles deposited on metallic or highly polarizable substrates could generate strong localized resonances near the gap between the particle and the substrate, which can be used to significantly enhance the PL.[5-6, 10] However, all the PL enhancement and polarization modulation of Au NPs has been limited to the achiral regime, mainly due to the lack of effective synthesis recipes of chiral structural Au NPs. It is necessary to extend the PL polarization manipulation picture to the chiral regime because chirality is an essential property in the field of chemistry, biology and pharmacy. Moreover, PL research has many potential applications in optical data storage, biosensing, displays etc.

Recently, a novel water-based bottom-up method has been reported, which enables the PL research to be expanded into the chiral realm. With the help of cysteine and cysteine-based peptide, various three-dimensional (3D) intrinsic right- and left-handed chiral as well as achiral NPs can be made.[11-14] These series chiral plasmonic NPs possess strong circular dichroism (CD) signals with the *g*-factor up to 0.2. Such chiroptical responses have been found to enhance and modulate some chiral activities at the single-particle level in nanophotonic system. One kinds of these gold nanohelicoids (GNH) was applied to effectively improve the valley-dependent PL contrast of a monolayer WS_2.[15] Photothermal dichroism was also realized by depositing the chiral nanoparticle on AlGaN: Er^{3+} film, which identified the optical and photothermal handedness.[16] However, the mechanism of gold nanohelicoid modulated chiroptical activities is not clear, though the single-particle chiral scatterometry[17] and hyper-Rayleigh scattering[18] of the GNH solution have been investigated. The study of the chiral PL properties of the GNH is expected to further elucidate the relationship between excitation/emission circular polarization and the handedness of chiral emitters in many chirality-related modulation and PL processes.

In this work, we comprehensively study, for the first time the chiral excitation and emission properties of chemically synthesized GNHs at the single-particle level. We observe that the PL emission of a single GNH is circularly polarized, and the signal intensity depends on the illumination handedness (i.e., left-circular polarization (LCP, σ^+) and right-circular polarization (RCP, σ^-)), leading to a PL intensity dissymmetry factor of 0.12. Moreover, we find that the emission polarization-resolved chiral PL signals show a preferential helicity to the excitation polarization, while the PL dissymmetry is steered either constructively or destructively. Finally, we employ two physical models to interpret these experimental observations, including a chiral PL phenomenological model for quantitatively evaluating the wavelength-dependent PL dissymmetry features and a chiral Purcell effect model for qualitatively interpreting the polarization-preserved emissions through the super-chiral near-fields in the GNHs.

2. Results and Discussion

2.1 Synthesis and Characterization of GNHs

In this work, GNH enantiomers were synthesized using a seed-mediated growth method with the guidance of L-/D- cysteine (Cys).[12] The left panels of **Figure 1a, b** show the scanning electron microscope (SEM) micrographs of left- and right-handed gold nanohelicoid (L-/R-GNH) structures and their corresponding 3D schematics (in the insets). In the right panels, the dashed lines illustrate opposite helicity of the two structures, where geometric chirality can be seen at both the surfaces and corners of the helicoids. **Figure 1c, d** depict the extinction and circular dichroism (CD) spectra of the left- and right-handed GNHs in an aqueous solution of CTAB, both showing agreement between simulation (dashed lines) and experimental results (solid lines). We can see from Figure 1c that the extinction cross section spectrum of the left-handed GNHs is dominated by a broadband electric dipole resonance peak from about 500 to 800 nm. Interestingly, the CD spectra for both left- and right-handed structures flip at about 610 nm (close to the experimental extinction peak at about 650 nm) and exhibit mirror-symmetric bisignate resonances with opposite handedness. The degree of the intrinsic structural chirality for the GNHs can be quantified by a CD *g*-factor, defined

as $g_{\mathrm{CD}} = 2\frac{A^+ - A^-}{A^+ + A^-}$, where A refers to the circular polarized extinction and the superscripts "+" and "-" represent the handedness of circular polarization excitation. The results in **Figure S1a** (Supporting Information) show that the maximum CD *g*-factors of the left- and right-handed GNHs are about -0.012 and 0.008, comparable to the values of ±0.01 reported in the literature.[12]

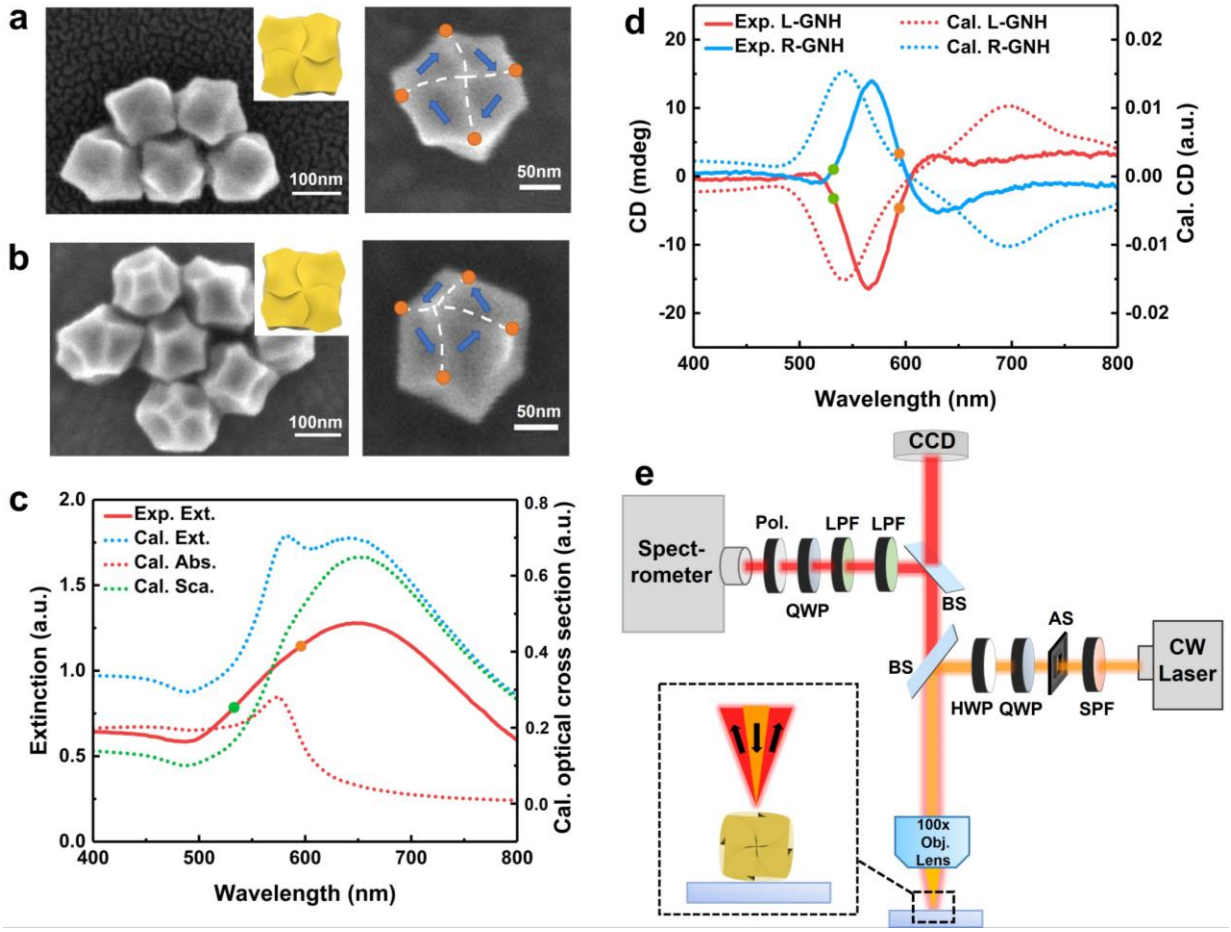

Figure 1. SEM micrographs of (a) left- and (b) right-handed gold nanohelicoid structures with an average size of 120-150 nm and insets are their corresponding 3D chiral schematics. Blue arrows and white dashed lines (connecting the orange vertices) in the right panels sketch opposite helicity of the two structures. (c) Experimental extinction (solid line) gold nanohelicoid structure in CTAB aqueous solution and simulated extinction, scattering and absorption (dashed lines) spectra of the left-handed gold nanohelicoid. (d) Experimental (solid lines) and simulated (dashed lines) CD spectra of the left- (L-GNH) and right-handed (R-GNH) structures. In the simulated spectra, the peak and dip at about 700 nm may be caused by the difference between the actual morphology and the simplified ideal model. (e) Schematic illustration of polarization-resolved dark-field scattering/PL measurements at the single-particle level. HWP: Half waveplate, QWP: Quarter waveplate, BS: Beam splitter, SPF: 600 nm short pass filter, LPF: 600 nm long pass filter, Pol.: Polarizer, AS: Aperture slot.

A home-built fluorescence microscope equipped with a polarization-resolved dark-field illumination module was used to measure the chiral scattering and PL spectra of individual GNHs. As sketched in **Figure 1e**, a continuous wave (CW) laser beam passes through a half and a quarter waveplate to produce circularly polarized light, which is then focused by a 100× objective lens to excite single GNHs (dispersed on an ITO glass substrate by a drop-casting method). The PL emission signal from the sample is collected by the same objective and sent to a spectrometer for spectral analysis and a CCD camera for image capture. A polarizer and a quarter waveplate are placed in front of the spectrometer to analyze the polarization state of the PL signal. Using the same microscope system equipped with a white light source, the chiral optical scatterometry of single GNHs can also be performed. The chiral scatterometry results shown in **Figure S1b, S1c in Supporting Information** reveal a clear difference in the circular polarized scattering intensities of a L-/R-GNH structure, indicating a sufficiently strong chiral response for observing chiral PL at the single-particle level.

2.2 Experimental Results of Chiral PL

To investigate the chiral excitation and emission properties of the GNHs, we first measured their PL spectra under circularly polarized excitation using the above experimental setup. The LCP and RCP illumination wavelength was set at 593.5 nm (close to the extinction peak of the GNHs, Figure 1c) to achieve plasmon-enhanced PL excitation. As shown in **Figure 2a**, the L-GNH structure exhibits a stronger PL signal in response to the RCP illumination than to the LCP one, while the PL signal of the right-handed R-GNH shows a reversed intensity contrast (**Figure 2b**). These results clearly reveal that the GNHs with opposite helicity have reversed absorptivity response to the RCP and LCP light. The dissymmetry factor of PL intensity is defined as $g_{\mathrm{PL}} = 2\frac{I^{+}-I^{-}}{I^{+}+I^{-}}$, where I refers to the emission PL intensity and the superscripts "+" and "-" represent the left- and right-handedness of excitation polarization. Accordingly, the g_{PL} for R- and L-GNHs is ±0.12, respectively. Moreover, we noticed that the PL spectra of either structures exhibit similar resonance and intensity characters with their scattering spectra (Figure S1b and S1c in Supporting

Information), all showing a broad peak at around 640 nm, and similar intensity contrast tendency in response to illumination light with opposite polarization handedness. As will be explained later, such PL-scattering similarity is because PL signals of Au NPs are usually dominated by plasmon-modulated and enhanced radiative recombination. To confirm the excitation polarization determined PL intensity contrast originating from the structural chirality of the GNHs, we also measured the scattering and PL spectra of an achiral gold nanocube of 100 nm in size: no scattering or PL intensity contrast is observed under the LCP and RCP illumination (**Figure S2a and S2b, Supporting information**).

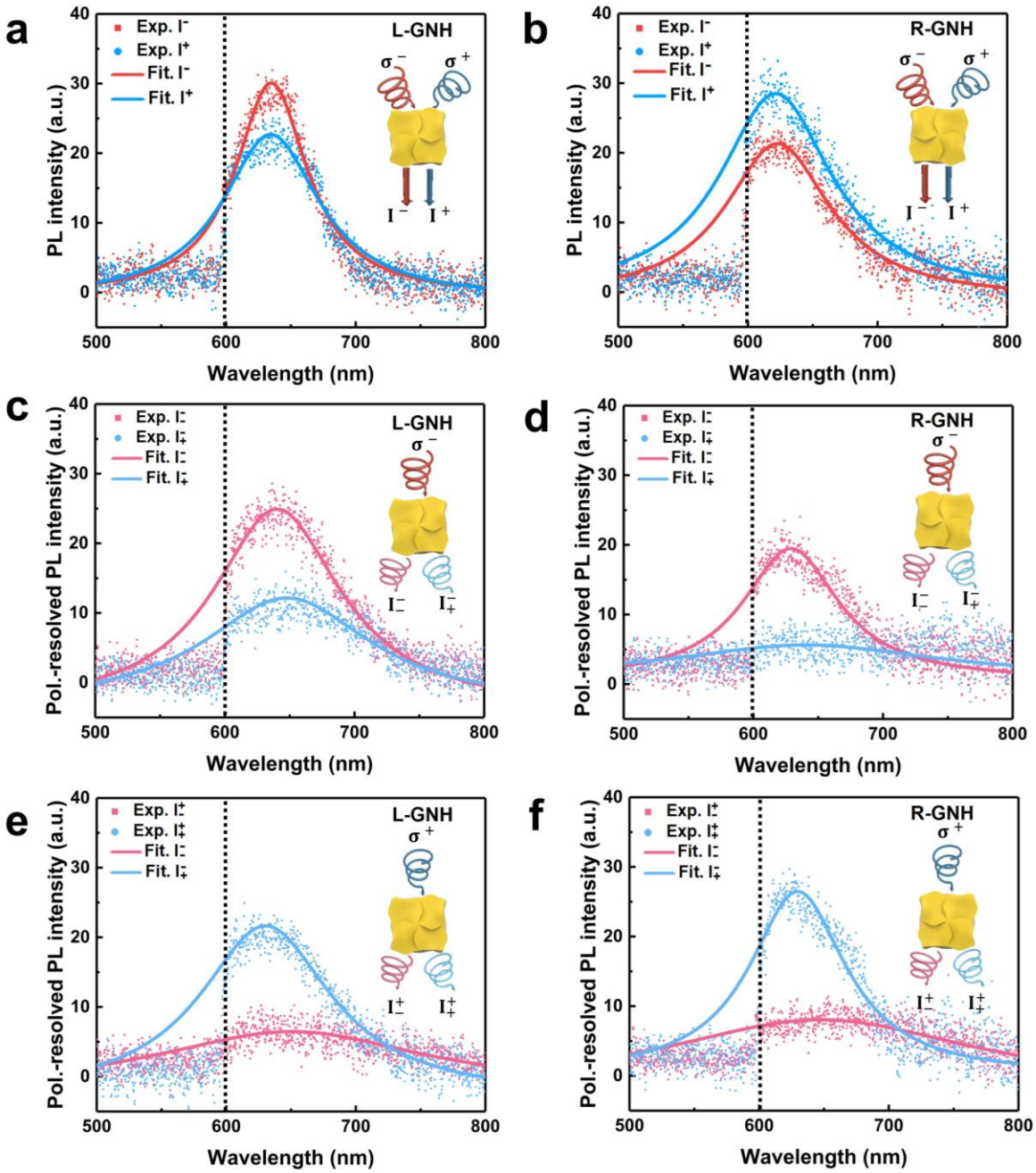

Figure 2. (a) PL spectra of a single left-handed (L-GNH) structure under RCP (σ^-, red) and LCP (σ^+, blue) laser illumination at 593.5 nm. (b) Similar results as (a) for a single right-handed Helicoid (R-GNH) structure. (c-f) Emission polarization-resolved PL spectra for the L-GNH (c, e) and R-GNH structures (d, f) under the RCP (c, d) and LCP (e, f) laser illumination at 593.5 nm. The PL intensity drop below 600 nm (black dashed line) is caused by the cut-off response of the long-pass filter used in the optical path. The solid lines in all spectra are Lorentz fits of the raw data.

To characterize the chiral properties of the measured PL signals for both GNHs in Figure 2a, 2b,

we decompose the PL signal into the LCP and RCP components by quarter-waveplate- polarizer combination. The decomposition results are summarized in **Figure 2c-f**. As can be seen, the dominant chiral component of the PL signal for each structure is the same as that of the illumination light, i.e., LCP (RCP) excitation generates LCP (RCP) component dominated PL regardless of the structural handedness of the GNHs. For a quantitative evaluation of the PL handedness, we calculated the chiral degree of polarization (DoP) of the measured polarization-resolved PL, i.e., so-called polarization-resolved PL *g*-factor, defined as $g_{\mathrm{RPL}} = 2\frac{I_+ - I_-}{I_+ + I_-}$, where *I* refers to emission polarization-resolved PL intensities and the subscripts "+" and "-" represent the handedness of emission polarization. Based on this definition, we find from Figure 2c that the absolute value of g_{RPL} for the L-GNH under the RCP illumination is about 0.55, which is much smaller than that for the R-GNH under the RCP illumination (1.03 for Figure 2d). However, the results for both structures under the LCP illumination reverses (1.04 for Figure 2e and 0.62 for Figure 2f). These comparison results imply the important role of structural chirality in the distinct chiral degrees of polarization. To confirm this, we also calculated the absolute value of g_{RPL} for the achiral gold nanocube particle (**Figure S2c and S2d** in Supporting Information). A same g_{RPL} value of 0.73 were found for both the RCP and LCP illumination conditions, indicating an excitation polarization independent g_{RPL} for an achiral structure without CD response. Compared with an achiral nanocube, the absolute g_{RPL} value of the GNH with co-/anti-chiral excitation is enhanced/suppressed, indicating a polarization-preserved phenomenon.

To extend our understanding of the chiral responses, the above measurements for the GNH enantiomers were also performed at an excitation wavelength of 532 nm. Compared with the excitation at 593.5 nm, the chiral PL and polarization-resolved chiral PL intensity of GNH under 532 nm illumination are much lower (**Figure S3, supporting information**). This can be attributed to the larger absorptivity of GNH at 593.5 nm (highlighted with an orange point, Figure 1c) with respect to that at 532 nm (highlighted with a green point), thus allowing more photons at 593.5 nm to participate in the whole PL process. Besides, the g_{PL} at 532 nm is also lower than that at 593.5

nm, which is in line with the observation in Figure 1d, that the GNH excited at 593.5 nm (marked with an orange point) shows larger absolute CD value than at 532 nm (marked with a green point). These observations ulteriorly suggest that the 593.5 nm light is more efficient for enhancement of the chiral PL response. Finally, the polarization-resolved chiral PL under 532 nm excitation presented in Figure S3c-f (Supporting Information) shows a similar scenario of the polarization-preserved PL as that of the 593.5 nm excitation.

2.3 The Mechanism of Chiral PL: A Chiral PL Phenomenological Model

To unveil the mechanism behind the above experimental results, then energy band structure of gold around the X point in the first Brillouin zone was depicted in **Figure 3a,** based on which the chiral PL mechanism was illustrated:

(1) Excitation. After absorbing the incident excitation photons, electrons near the top of the *d*-band are excited into the upper *sp*-band, with holes left at the top of the *d*-band.[1] The absorption probability $Y_{abs}(\omega_{ex})$ is used to describe the probability of a single photon absorbed by materials at the excitation frequency ω_{ex}. The pumping rate $P_{\pm}$ of the single-photon PL process is determined by the local electric field intensity $I(\omega_{ex})$. In our case, the single GNHs show dramatically different optical absorptivity when excited with circularly polarized light with opposite handedness. We can take the L-GNH as an example. In light of its negative CD value at around 593.5 nm (Figure 1d), it prefers to absorb RCP light, meaning more electrons can be excited into the upper *sp*-band (Figure 3a).

(2) Relaxation. Subsequent to the upward electron excitation, the energetic electrons experience a nonradiative thermalization process, which gives rise to a broad distribution of electron energies. The population of the excited electrons relaxing to a specific emission state with angular frequency ω_{em} is determined by the relaxation probability $Y_r(\omega_{em})$.

(3) Emission. Finally, the excited electrons either directly recombine with the *d*-band holes, and simultaneously emit photons, or excite the localized surface plasmon of metal nanostructures. The LSP typically decays in both the nonradiative (via ohmic loss) and radiative (far-field radiation) ways. For nanostructured noble metals, most of the PL emission originates from the radiative

plasmon damping, while a small percentage is from the direct recombination of the energetic electrons with the holes left in the *d*-band.[2, 4-5, 21] The photon emission probability is denoted as $Y_{em}(\omega_{em})$, and the emission oscillation orientation is reconstructed by the excitation polarization state and influenced by the chiral morphology of the GNH. [22-24]

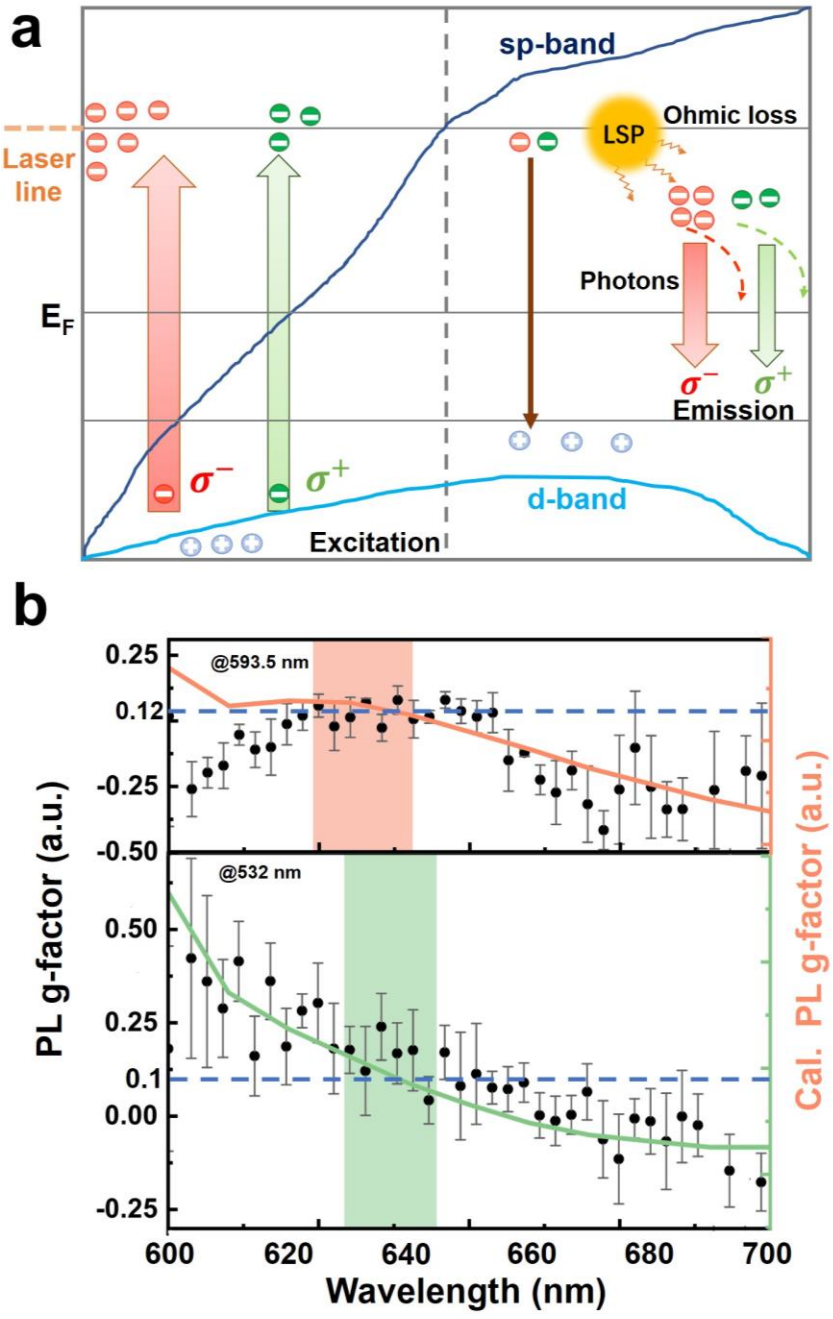

Figure 3. (a) Schematic illustration of the chiral PL mechanism of the chiral nanostructures. Here take the L-GNH as an example. Th excitation wavelength is 593.5 nm. The RCP light (red thick upward arrow) excites more

d-band electrons of gold to the *sp*-band due to its larger absorptivity compared to that of the LCP light (green thinner upward arrow). Most of the energetic electrons transfer to the LSP band while a minority of them directly recombine with the holes (brown thin downward arrow). Then, the excited LSPs undergo either radiative decay to generate PL emission (red and green dashed arrows) or non-radiative decay resulting in Ohmic loss. The PL emission can be modulated by the structural chirality of the GNH. (b) Chiral PL *g*-factors for the L-GNH structure under near-resonant 593.5 nm (upper panel) and off-resonant 532 nm (lower panel) excitations. Black dots are experimental data while orange and green lines are calculation results. Blue dashed lines indicate the averaged *g*-factor at the PL peaks (shadowed areas): 0.12 for the 593.5 nm excitation and 0.1 for the 532 nm excitation.

Based on the above discussions, the single-photon absorption induced luminescence of gold can be quantitively evaluated by a phenomenological model. Specifically, the chiral PL intensity from an elementary volume dV is defined as:[25]

$$I_{\mathrm{PL-d}V}(\omega_{\mathrm{ex}}) = I(\omega_{\mathrm{ex}})Y_{\mathrm{abs}}(\omega_{\mathrm{ex}})Y_{\mathrm{r}}(\omega_{\mathrm{em}})Y_{\mathrm{em}}(\omega_{\mathrm{em}}) \quad (1)$$

In a phenomenological way, Equation (1) can be simplified and modified based on the following considerations: (i) The excitation intensity $I(\omega_{\mathrm{ex}})$ at a local elementary volume is $|E_{\mathrm{loc}}(\omega_{\mathrm{ex}})|^2$; (ii) The absorption probability $Y_{\mathrm{abs}}(\omega_{\mathrm{ex}})$ and relaxation probability $Y_{\mathrm{r}}(\omega_{\mathrm{em}})$ are constants and associated with the imaginary part of the permittivity of gold; (iii) The emission probability of radiative recombination $Y_{\mathrm{em}}(\omega_{\mathrm{em}})$ is determined by the local field density of optical states (LDOS), which is proportional to the field intensity at the emission frequency $|E_{\mathrm{loc}}(\omega_{\mathrm{em}})|^2$.[26] Based on the above assumptions, the relative chiral PL intensity of helicoids with different handedness given in Equation (1) can be written as:

$$I_{\mathrm{PL}}^{\mathrm{relative}}(\omega_{\mathrm{ex}}) = \int |E_{\mathrm{loc}}(\omega_{\mathrm{ex}})/E_0(\omega_{\mathrm{ex}})|^2 \cdot |E_{\mathrm{loc}}(\omega_{\mathrm{em}})/E_0(\omega_{\mathrm{em}})|^2 \mathrm{d}V \quad (2)$$

where E_0 is the background electric field intensity. Thus, the relative chiral PL intensity can be evaluated by the electric fields respectively at the excitation and emission frequencies, which can be retrieved from numerical simulations. As shown in the **Figure 3b**, the calculated (orange line) g_{PL} spectra of L-GNH at 593.5 nm illumination and at 532 nm illumination (green line) agree well with the experimental data (black line). The results indicate the dissymmetry feature of chiral nanohelicoids originates from the different spatial overlapping profile of local electric enhancement field distributions under excitation and emission.

2.4 Super-Chiral Near Fields and a Chiral Purcell Effect Model

On the strength of the discussion above, the chiral PL intensity contrast is caused by both excitation polarization induced GNHs' absorption difference and spatial electrical field overlap profile of the excitation and emission light. To unveil how the local field of GNHs affects the polarization-resolved chiral PL shown in Figure 2c-f, the numerical calculation of local fields based on FDTD solution is performed using simplified structural GNH models. **Figure 4a, b** depict the simulated electric and magnetic near-field distributions in the middle-plane cross section of the chiral nanostructure (sketched in **Figure S5a**, Supporting Information). Figure **S5b, S5c** (Supporting information) renders the calculated electric and magnetic near-field intensity difference for the R-GNH structure under left- and right-handed circular polarized excitation which manifests that the intrinsic structural chirality of the GNH attributes to its chiral optical response.

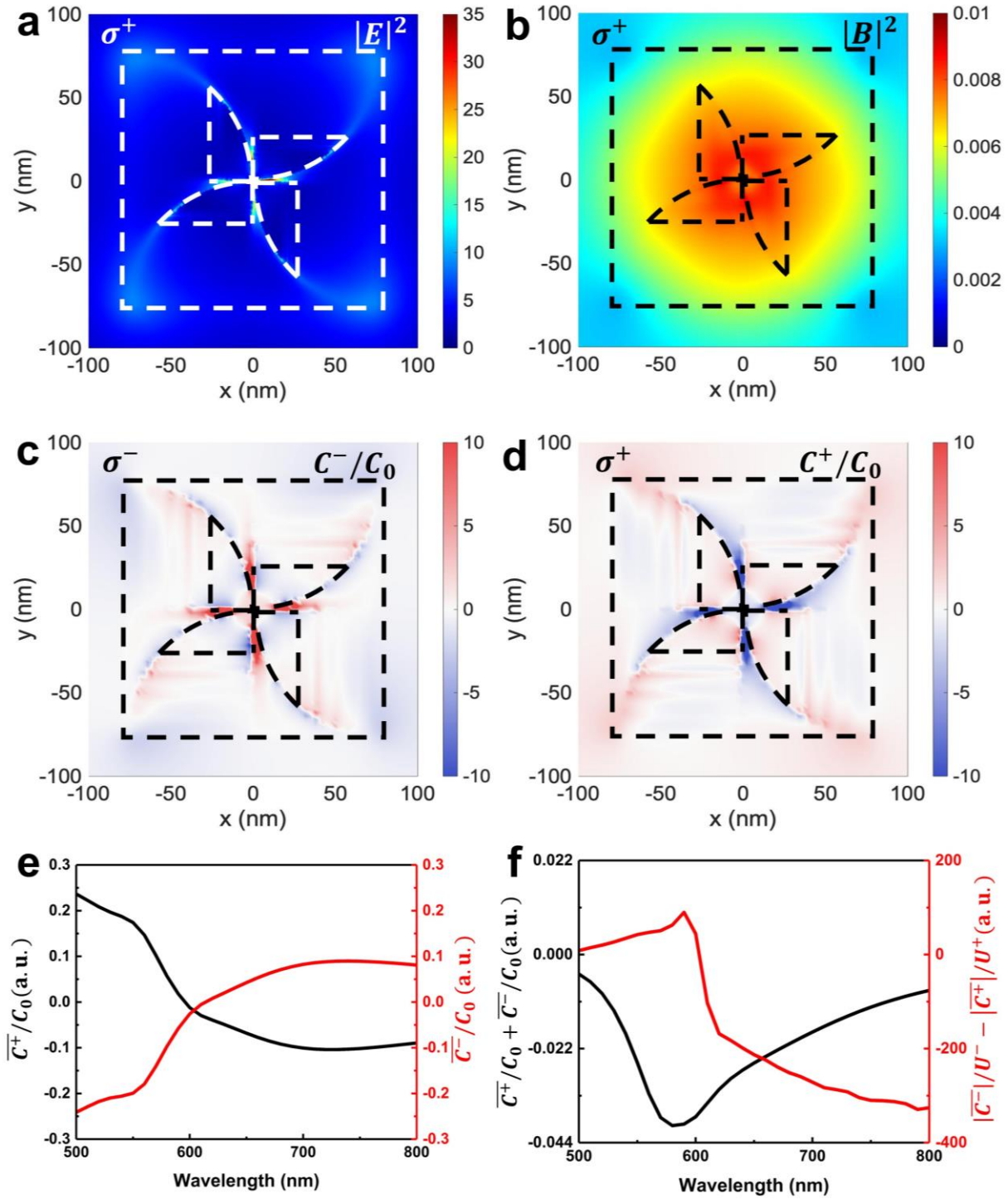

Figure 4. (a, b) Simulated (a) electric and (b) magnetic near-field intensity distribution for an R-GNH under 593.5 nm LCP illumination. (c, d) Calculated near-field chirality distribution in the R-GNH under 593.5 nm (c) LCP and (d) RCP illumination. (e) The integrated net optical chirality for a left-handed helicoid under RCP (red) and LCP (black) excitation. (f) The sum of integrated optical chirality for GNHs under RCP and LCP excitation, $\frac{\overline{C^+}}{C_0} + \frac{\overline{C^-}}{C_0}$. The non-zero value corresponds to the chiral antenna mode of the GNHs, with the largest dissymmetry

factor appeared at around 600 nm. The parameter $\frac{|\overline{C^-}|}{U^-} - \frac{|\overline{C^+}|}{U^+}$ is minus for λ > 600 nm, which indicates the polarization-preserved effect in polarization-resolved PL.

The local optical chirality is used to quantify the superchiral field and its light interactions in an optical cavity.[27-29] The near field distribution of the optical chirality is expressed as a pseudoscalar according to the symmetry of time and parity:[30-31] $C(\boldsymbol{r}) = -\frac{\varepsilon_0 \omega}{2} \mathrm{Im}[\boldsymbol{E}^*(\boldsymbol{r}) \cdot \boldsymbol{B}(\boldsymbol{r})]$, where $\boldsymbol{E}$, $\boldsymbol{B}$, ε_0, ω, are the electric field, magnetic field, permittivity of vacuum and the angular frequency, respectively. This term can be treated as a chiral analogue to the LDOS, and indicates enhancement of chirality of the local field.[32] As shown in **Figure 4c, d**, the simulated near-field distribution of optical chirality exhibit asymmetric patterns under circularly polarized light illumination. For the LCP (RCP) illumination condition, the chiral field inside the GNHs (dashed 'pinwheel' pattern) and at the corners of the GNHs show positive (negative) C/C_0, where C_0 is the value of optical chirality of circularly polarized light without GNHs. A maximum optical chirality around ± 8 is obtained inside the left- and right-handed GNH hot spots, indicating strong local chiral enhancement.

The integration of the optical chirality inside GNHs is performed to get the spectral net optical chirality $\bar{C}$ (**Figure 4e**). With reversed excitation polarizations, the signs of net optical chirality are opposite, which is in line with the flips of the dominant components shown in Figure 2c-f. The net optical chirality feature at 600 nm is also in compliance with CD spectrum in Figure 1d as the absorption rate is closely related to C:[25] $\mathrm{CD}(\boldsymbol{r}) = -\frac{4G''}{\varepsilon_0} C(\boldsymbol{r})$, where $G''$is the imaginary part of isotropic mixed electric-magnetic dipole polarizability G.[33]

In addition, the optical chirality in the near-field determines the polarization character of the far-field PL via so-called chiral Purcell effect, which is responsible for the g_{RPL} obtained in experiment (Figure 2c-f).[34-36] The GNHs' chiral PL is modeled as uniformly distributed chiral emitters inside the GNH cavity with excitation determined polarization and modified spontaneous decay rate. The

chirality of the emitter can be described by the contrast of polarization-resolved PL from an achiral nanocube of the same size as our GNHs. Its dissymmetry factor can be written as: $g_{\mathrm{A}}{}^{\pm} = 2\frac{I_{\mathrm{A}+}{}^{\pm} - I_{\mathrm{A}-}{}^{\pm}}{I_{\mathrm{A}+}{}^{\pm} + I_{\mathrm{A}-}{}^{\pm}}$. The spontaneous decay rate is modified by chiral Purcell equation:[22] $\frac{\Delta\Gamma(\boldsymbol{r})}{\Delta\Gamma_0} = F_C \frac{\omega_0^2}{\omega^2}\frac{\omega_0^2}{\omega_0^2+4Q^2(\omega-\omega_0)^2}\frac{C(\boldsymbol{r})}{C_{\max}}\eta_{\mathrm{c}} \propto -\frac{C(\boldsymbol{r})}{\omega^3 U}$, where $\Delta\Gamma(\boldsymbol{r}) = \Gamma^+(\boldsymbol{r}) - \Gamma^-(\boldsymbol{r})$ represents the differential decay of a chiral dipole emitter coupled to the σ^+ and σ^- circularly polarized modes of the optical cavity at frequency ω. $\Delta\Gamma_0$, F_{C}, ω_0, Q, $C(\boldsymbol{r})$, $C_{\max}$, η_{C}, and U are the unmodified differential decay, the chiral Purcell factor, the resonant frequency, the quality factor of the optical cavity, local optical chirality, maximum optical chirality, exciton orientation factor, and total energy of the cavity respectively. In our case, the enhanced/suppressed g_{RPL} of polarization-resolved PL generated from hot spots in GNHs under opposite handedness excitation can be derived as:

$$|g^+| = 2\left|\frac{I_{\mathrm{A}+}{}^{+} - I_{\mathrm{A}-}{}^{+} + \alpha}{I_{\mathrm{A}+}{}^{+} + I_{\mathrm{A}-}{}^{+} - \alpha}\right|$$

$$|g^-| = 2\left|\frac{I_{\mathrm{A}-}{}^{-} - I_{\mathrm{A}+}{}^{-} + \beta}{I_{\mathrm{A}-}{}^{-} + I_{\mathrm{A}+}{}^{-} - \beta}\right|$$

where $\alpha = \frac{|\overline{C^+}| - |\overline{C^-}|\frac{U^+}{U^-}}{|\overline{C^+}|} I_{\mathrm{A}-}{}^{+}$ and $\beta = \frac{|\overline{C^-}| - |\overline{C^+}|\frac{U^-}{U^+}}{|\overline{C^-}|} I_{\mathrm{A}+}{}^{-}$. When $\lambda > 600$ nm we have: $\frac{|\overline{C^-}|}{U^-} - \frac{|\overline{C^+}|}{U^+} < 0$, as shown in **Figure 4f**. Consequently, $\alpha > 0$ and $\beta < 0$, which suggest $|g^+| > |g_{\mathrm{A}}|$ and $|g^-| < |g_{\mathrm{A}}|$, respectively (For details see **Methods**).

In the above process, the asymmetric chiral response of the GNHs can also be understood by the chiral antenna effect. Under linearly polarization excitation, GNHs' resonant scattering response can be separated in the far field domain with numerical method ($E_{\mathrm{LCP}} = E_x + iE_y$ and $E_{\mathrm{RCP}} = E_x - iE_y$). The dissymmetry contrast is calculated and plotted in **Figure S6** (Supporting Information), which is in accordance with the net optical chirality under isotropic excitation (Figure 4f, $\frac{C_{\mathrm{isotropic}}}{C_0} = \frac{\overline{C^+}}{C_0} + \frac{\overline{C^-}}{C_0}$), both showing a dip at 600 nm. The GNHs' chiral antenna emission process is also conducted experimentally by using linearly polarized light (593.5 nm and 532 nm) to excite the CPL signal of GNHs (**Figure S7**, Supporting Information). L-GNH exhibit larger RCP PL than that of LCP, while R-GNH showed a reverse scenario. Treating the linearly polarized excitation as

a superposition of two excitations with opposite handedness, the enhancement and suppression g_{RPL} in experimental polarization-resolved chiral PL results shown in Figure 2 can be further confirmed via CPL results as obtained above. Although the intensity varies, the contrast and polarization property of chiral PL signals obtained under the 593.5 nm and 532 nm excitation conditions reflect the same trend, which indicates a similar chiral-antennas-like behavior of GNHs at wavelengths ranging from 600 to 750 nm.

Additionally, to further understand the impact of morphology on chiral PL signal, the same experiments were done on gold nanohelicoid with another structure (left-handed gold nanohelicoid II, GNH II), which are discussed in Supporting Information the 'Geometric Handedness Dependent Chiral PL' section. The results reveal that the chiral PL response of gold helicoid is closely related to its intrinsic chiroptical activities, i.e., stronger chiroptical responses lead to stronger chiral PL, manifesting that the chiral PL can be improved by GNH with higher chiroptical activity in the future.

3. Conclusion

In conclusion, we experimentally studied the chiral PL properties of GNH at the single-particle level. It was observed that, the exhibited PL signals of GNH enantiomers show a reverse intensity trend in light of circular dichroism absorption, while the polarization-resolved chiral PL signal is circular polarization-preserved. Phenomenological model quantifies the dissymmetry *g*-factor of chiral PL, showing good agreement with our experimental results. The simulated optical super-chiral near field validates that GNH acts as a chiral antenna via chiral Purcell effect, and results in preferred emission of polarization-resolved chiral PL signal. Our results suggest that the scattering and PL of chiral nanostructures have single-particle level circular differential performance and specific preferential emission helicity, further boosting their underlying use in the field of chirality-related biology displays, sensing and probing.

4. Methods

Synthesis of Gold Chiral Structure

Synthesis of Gold Seeds: For the synthesis of small 2-nm-sized spherical gold seed nanoparticles, 0.25 mL 10 mM tetrachloroauric (iii) trihydrate ($HAuCl_4$) was added to 7.5 mL 100 mM Hexadecyltrimethylammonium bromide (CTAB), then 0.8 mL 10 mM sodium borohydride ($NaBH_4$) was rapidly injected into the mix solution. The dark brown solution was aged at 28 ℃ for 3 h.[9]

Synthesis of Cubic Seed Gold Nanoparticles: For the preparation of large cubic seed gold nanoparticles, 55 μL 1/10 diluted spherical gold seeds were added to the growth solution, which contained 8 mL deionized (DI) water, 0.2 mL $HAuCl_4$ (10 mM), 1.6 mL CTAB (100 mM) and 0.95 ml 50 mM ascorbic acid (AA). The final solution turned pink after 15 min. The resultant cubic gold nanoparticles were centrifuged twice and redispersed in 1 mM CTAB solution.[37]

Synthesis of Chiral Gold Nanoparticles: For the synthesis of GNHs the growth solution was prepared by mixing 3.95 mL DI water, 0.8 mL CTAB (100 mM), 0.475 mL 100 mM AA, 0.1 mL $HAuCl_4$, and 5 μL 100 μM L/D-cys. With the addition of 100 μL premade cubic nanoparticles, the synthesis of nanohelicoids started at 28 ℃ and continued for 1 h. Centrifugation was carried out twice, and after removing unreacted chemicals, the chiral nanoparticles were stored in 1 mM CTAB solution for further measurement.[11-12]

Sample Preparation and Characterization The chiral nanoparticles were rinsed and diluted with DI water. One drop of diluted solution (~20 μL) was casted onto ITO glass. Upon drying in air, most monomers of GNHs were dispersed with large particle-particle separations, allowing for single nanoparticle measurement. Absorption and CD spectra were recorded by a J-1500 Circular Dichroism Spectrophotometer (JASCO). SEM images were taken by Field Emission Scanning Electron Microscope (Tescan MAIA3).

Single-particle Chiral PL Spectroscopy and Chiral Scatterometry A linearly polarized monochromatic CW laser with wavelength of 532/593.5 nm (MGL-F-593.5-100mW/ MGL-III-532-100mW, CNI Co., Ltd.) was selected as the excitation source and a quarter-half waveplate combination was used to generate circularly polarized light. As shown in Figure S12, the half waveplate (HWP, AHWP05M-600 Thorlabs Inc.) was used to eliminate the depolarization effect

of the beam splitter (BS, BSW10R, Thorlabs Inc.) in the excitation path, by rotating to a specific orientation angle with respect to the fast axis of the quarter wave plate (QWP, AQWP05M-600 Thorlabs Inc.). The evaluation of the polarization degree of the optic setup is discussed in Supporting Information. The aperture slot (SM1D12D, Thorlabs Inc.) in front of the laser was used as a spatial filter to optimize the quality of the laser beam. The followed short pass filter (FES0600, Thorlabs Inc.) was to cancel out the side band effect of the 593.5 nm laser. When doing the experiment, each GNH was aligned to the center of the laser spot using a three-axis piezo-controlled stage. The laser power was set at ~80 μW to excite PL signal. A 100× microscope (LMPlan FL N 100× 0.80, Olympus) with numerical aperture of 0.8 was used to focus the incident laser beam and collected the PL or scattering light from the sample. The signal integration time is 20s. Every signal collection was done three times. The polarization effect of the beam splitter inside the microscope was removed by a polarization calibration. Two 600 nm long pass filters (FES0600, Thorlabs Inc.) were used to block the 532/593.5 nm excitation, and an imaging spectrometer (Acton Sp2300, Princeton Instruments spectrometer integrated with PIXIS 400 CCD camera) was used to record the signal. When the chiral scatterometry measurement was carried out, the light source is switched to a white light lamp.

Electromagnetic Simulation The Lumerical FDTD solution package was used to simulate the scattering/absorption/extinction cross section, near-field distribution of electric/magnetic/optical chirality field and far-field separation of chiral components. A simplified geometry model was used in the simulation to mimic the key structure features of that used in experiment, which has been validated by previous work.[8] In the FDTD model, the circular polarized plane wave was created by superposing two linearly polarized plane waves with a phase difference of ± 90 degree was used as excitation. The near-field monitor was placed beneath the surface of GNHs to record the field distribution. The relative PL intensity and integration of local optical chirality were calculated using the same 3D geometry model but meshed with the COMSOL software. It should be noticed that, there is a red shift of the CD peak between the simulation and experiment result at about 610 nm. This is because the 3D model used in simulation is a simplified model with one size while the

experiment CD is measured in gold nanohelicoid solution with the size ranging from 120-150 nm. ***Chiral Purcell Effect Model*** According to previous work, the modification factor of chiral molecule can be expressed via chiral Purcell effect by:[31] $M(\boldsymbol{r}) = \frac{\Delta\Gamma(\boldsymbol{r})}{\Delta\Gamma_0} \propto -\frac{C(\boldsymbol{r})}{\omega^3 U}$. For opposite circular polarization, due to the spin-photon locking effect, i.e., $\frac{{\Gamma_0}^+(\boldsymbol{r})-{\Gamma_0}^-(\boldsymbol{r})}{{\Gamma_0}^+(\boldsymbol{r})+{\Gamma_0}^-(\boldsymbol{r})} = \pm 1$, the chiral Purcell equation can be written as:

$$M^{\pm}(\boldsymbol{r}) = \frac{\Gamma^{\pm}(\boldsymbol{r})}{\Gamma_0} \propto -\frac{C^{\pm}(\boldsymbol{r})}{\omega^3 U^{\pm}}$$

where the superscript represents the excitation polarization state. The chiral PL of GNHs is modeled as uniformly distributed chiral emitters inside the structure with excitation determined polarization and spontaneous decay rate as modified above. The chirality of the emitter can be described by the contrast of polarization-resolved PL from an achiral nanocube of 100 nm size. This dissymmetry factor can be written as: ${g_{\mathrm{A}}}^{\pm} = 2\frac{{I_{\mathrm{A}+}}^{\pm} - {I_{\mathrm{A}-}}^{\pm}}{{I_{\mathrm{A}+}}^{\pm} + {I_{\mathrm{A}-}}^{\pm}}$, where ${I_{\mathrm{A}\pm}}^{\pm}$ are the intensity of opposite chiral components of achiral nanocube PL under opposite chiral excitation. According to symmetry of achiral nanocube under opposite excitation, we have ${g_{\mathrm{A}}}^{+} = -{g_{\mathrm{A}}}^{-}$, that is, ${I_{\mathrm{A}+}}^{+} = {I_{\mathrm{A}-}}^{-}$ and ${I_{\mathrm{A}-}}^{+} = {I_{\mathrm{A}+}}^{-}$, respectively. Consequently, $|{g_{\mathrm{A}}}^{\pm}|$ is about $\frac{1}{3}$ in Figure S2c, S2d (supporting information). The modified asymmetry in spontaneous emission of GNH under opposite excitation can be calculated as:

$$g^{\pm}(\boldsymbol{r}) = 2\frac{{I_+}^{\pm} - {I_-}^{\pm}}{{I_+}^{\pm} + {I_-}^{\pm}} = 2\frac{\Gamma^+(\boldsymbol{r}){I_{\mathrm{A}+}}^{\pm} - \Gamma^-(\boldsymbol{r}){I_{\mathrm{A}-}}^{\pm}}{\Gamma^+(\boldsymbol{r}){I_{\mathrm{A}+}}^{\pm} + \Gamma^-(\boldsymbol{r}){I_{\mathrm{A}-}}^{\pm}} = 2\frac{C^+(\boldsymbol{r}){I_{\mathrm{A}+}}^{\pm}/U^+ - C^-(\boldsymbol{r}){I_{\mathrm{A}-}}^{\pm}/\mathrm{U}^-}{C^+(\boldsymbol{r}){I_{\mathrm{A}+}}^{\pm}/U^+ + C^-(\boldsymbol{r}){I_{\mathrm{A}-}}^{\pm}/\mathrm{U}^-}$$

We use a spatially averaged net value of optical chirality to consider an overall effect for $\lambda >$ 600nm:

$$g^{\pm} = 2\frac{|\overline{C^+}|{I_{\mathrm{A}+}}^{\pm}/U^+ - |\overline{C^-}|{I_{\mathrm{A}-}}^{\pm}/U^-}{|\overline{C^+}|{I_{\mathrm{A}+}}^{\pm}/U^+ + |\overline{C^-}|{I_{\mathrm{A}-}}^{\pm}/U^-}$$

which can be expanded in the following form:

$$|g^+| = 2\left|\frac{{I_{A+}}^+ - {I_{A-}}^+ + \frac{\left|\overline{C^+}\right| - |\overline{C^-}|\frac{U^+}{U^-}}{\left|\overline{C^+}\right|}{I_{A-}}^+}{{I_{A+}}^+ + {I_{A-}}^+ + \frac{-\left|\overline{C^+}\right| + |\overline{C^-}|\frac{U^+}{U^-}}{\left|\overline{C^+}\right|}{I_{A-}}^+}\right| = 2\left|\frac{{I_{A+}}^+ - {I_{A-}}^+ + \alpha}{{I_{A+}}^+ + {I_{A-}}^+ - \alpha}\right|$$

$$|g^-| = 2\left|\frac{{I_{A-}}^- - {I_{A+}}^- + \frac{|\overline{C^-}| - \left|\overline{C^+}\right|\frac{U^-}{U^+}}{|\overline{C^-}|}{I_{A+}}^-}{{I_{A-}}^- + {I_{A+}}^- + \frac{-|\overline{C^-}| + \left|\overline{C^+}\right|\frac{U^-}{U^+}}{|\overline{C^-}|}{I_{A+}}^-}\right| = 2\left|\frac{{I_{A-}}^- - {I_{A+}}^- + \beta}{{I_{A-}}^- + {I_{A+}}^- - \beta}\right|$$

where $\alpha = \frac{|\overline{C^+}| - |\overline{C^-}|\frac{U^+}{U^-}}{|\overline{C^+}|}{I_{A-}}^+$ and $\beta = \frac{|\overline{C^-}| - |\overline{C^+}|\frac{U^-}{U^+}}{|\overline{C^-}|}{I_{A+}}^-$. For R-GNHs, we have: $\frac{|\overline{C^+}|}{U^+} - \frac{|\overline{C^-}|}{U^-} < 0$ as shown in Figure 4f. Consequently, we have $\alpha > 0$ and $\beta < 0$ and accordingly:

$$|g^+| = 2\left|\frac{{I_{A+}}^+ - {I_{A-}}^+ + \alpha}{{I_{A+}}^+ + {I_{A-}}^+ - \alpha}\right| > 2\left|\frac{{I_{A+}}^\pm - {I_{A-}}^\pm}{{I_{A+}}^\pm + {I_{A-}}^\pm}\right| = |g_A|$$

$$|g^-| = 2\left|\frac{{I_{A-}}^- - {I_{A+}}^- + \beta}{{I_{A-}}^- + {I_{A+}}^- - \beta}\right| < 2\left|\frac{{I_{A+}}^\pm - {I_{A-}}^\pm}{{I_{A+}}^\pm + {I_{A-}}^\pm}\right| = |g_A|$$

Consequently, this result indicates the enhancement/suppression of dissymmetry factors in Figure 2c-f.

Acknowledgements

H. Gao and P. G. Chen contributed equally to this work. We acknowledge the financial support from the Research Grants Council of Hong Kong (GRF Grant No. 152603/16E and CRF Grant No. C6013-18G). We thank Mr. Yunkun Xu for his useful discussion on COMSOL simulation and Dr. Guangcan Li for his careful polishing of the manuscript.

Conflict of Interest

The authors declare no conflict of interest.

References

[1] A. Mooradian, *Phys. Rev. Lett.* **1969**, 22, 185.

[2] D. Huang, C. P. Byers, L.-Y. Wang, A. Hoggard, B. Hoener, S. Dominguez-Medina, S. Chen, W.-S. Chang, C. F. Landes, S. Link, *ACS Nano* **2015**, 9, 7072.

[3] Y. Cheng, G. Lu, Y. He, H. Shen, J. Zhao, K. Xia, Q. J. N. Gong, *Nanoscale* **2016**, 8, 2188.

[4] H. Hu, H. Duan, J. K. Yang, Z. X. Shen, *ACS Nano* **2012**, 6, 10147.

[5] G. C. Li, Y. L. Zhang, J. Jiang, Y. Luo, D. Y. Lei, *ACS Nano* **2017**, 11, 3067.

[6] C. Lumdee, B. Yun, P. G. Kik, *ACS Photonics* **2014**, 1, 1224.

[7] W. Zhang, Y. Cheng, J. Zhao, T. Wen, A. Hu, Q. Gong, G. Lu, *J. Phys. Chem. C* **2019**, 123, 9358.

[8] X. Wu, T. Ming, X. Wang, P. Wang, J. Wang, J. Chen, *ACS Nano* **2010**, 4, 113.

[9] W. Rao, Q. Li, Y. Wang, T. Li, L. Wu, *ACS Nano* **2015**, 9, 2783.

[10] A. Tittl, X. Yin, H. Giessen, X.-D. Tian, Z.-Q. Tian, C. Kremers, D. N. Chigrin, N. J. N. l. Liu, *Nano Lett* **2013**, 13, 1816.

[11] H. E. Lee, H. Y. Ahn, J. Mun, Y. Y. Lee, M. Kim, N. H. Cho, K. Chang, W. S. Kim, J. Rho, K. T. Nam, *Nature* **2018**, 556, 360.

[12] H. E. Lee, R. M. Kim, H. Y. Ahn, Y. Y. Lee, G. H. Byun, S. W. Im, J. Mun, J. Rho, K. T. Nam, *Nat. Commun.* **2020**, 11, 263.

[13] Y. Y. Lee, N. H. Cho, S. W. Im, H. E. Lee, H. Y. Ahn, K. T. J. C. Nam, *Chem. Nano. Mat.* **2020**, 6, 362.

[14] N. H. Cho, G. H. Byun, Y. C. Lim, S. W. Im, H. Kim, H. E. Lee, H. Y. Ahn, K. T. Nam, *ACS Nano* **2020**, 14, 3595.

[15] S. Kim, Y. C. Lim, R. M. Kim, J. E. Fröch, T. N. Tran, K. T. Nam, I. J. S. Aharonovich, *Small* **2020**, 16, 2003005.

[16] A. Rafiei Miandashti, L. Khosravi Khorashad, M. E. Kordesch, A. O. Govorov, H. H. Richardson, *ACS Nano* **2020**, 14, 4188.

[17] J. Karst, N. H. Cho, H. Kim, H. E. Lee, K. T. Nam, H. Giessen, M. Hentschel, *ACS Nano*

2019, 13, 8659.

[18] L. Ohnoutek, N. H. Cho, A. W. Allen Murphy, H. Kim, D. M. Răsădean, G. D. Pantoş, K. T. Nam, V. K. J. N. l. Valev, *Nano Lett* **2020**, 20, 5792.

[19] J. P. Riehl, F. S. Richardson, *Chem. Rev.* **1986**, 86, 1.

[20] Y. Sang, J. Han, T. Zhao, P. Duan, M. Liu, *Adv.Mater.* **2020**, 32, 1900110.

[21] S. K. Andersen, A. Pors, S. I. Bozhevolnyi, *ACS Photonics* **2015**, 2, 432.

[22] T. Yin, L. Jiang, Z. Dong, J. K. Yang, Z. X. Shen, *Nanoscale* **2017**, 9, 2082.

[23] L. Jiang, T. Yin, Z. Dong, H. Hu, M. Liao, D. Allioux, S. J. Tan, X. M. Goh, X. Li, J. K. Yang, *ACS Photonics* **2015**, 2, 1217.

[24] T. Yin, L. Jiang, Z. J. C. P. B. Shen, *Chin.Phys.B* **2018**, 27, 097803.

[25] M. R. Beversluis, A. Bouhelier, L. Novotny, *Phys. Rev. B* **2003**, 68, 115433.

[26] S. Viarbitskaya, A. Teulle, R. Marty, J. Sharma, C. Girard, A. Arbouet, E. Dujardin, *Nat. Mater.* **2013**, 12, 426.

[27] Y. Tang, A. E. Cohen, *Science* **2011**, 332, 333.

[28] E. Hendry, T. Carpy, J. Johnston, M. Popland, R. Mikhaylovskiy, A. Lapthorn, S. Kelly, L. Barron, N. Gadegaard, M. Kadodwala, *Nat. Nanotechnol.* **2010**, 5, 783.

[29] A. O. Govorov, Z. Fan, P. Hernandez, J. M. Slocik, R. R. J. N. l. Naik, *Nano Lett* **2010**, 10, 1374.

[30] S. Yoo, Q.-H. Park, *Phy. Rev. Lett.* **2015**, 114, 203003.

[31] Z. Wu, J. Li, X. Zhang, J. M. Redwing, Y. Zheng, *Adv.Mater.* **2019**, 31, 1904132.

[32] L. V. Poulikakos, P. Thureja, A. Stollmann, E. De Leo, D. J. J. N. l. Norris, *Nano Lett* **2018**, 18, 4633.

[33] Y. Tang, A. E. Cohen, *Phy. Rev. Lett.* **2010**, 104, 163901.

[34] Z. Wang, Y. Wang, G. Adamo, J. Teng, H. Sun, *Laser & Photonics Rev.* **2019**, 13, 1800276.

[35] W. Du, X. Wen, D. Gérard, C.-W. Qiu, Q. J. S. C. P. Xiong, Mechanics, Astronomy, *Science China Physics, Mechanics & Astronomy* **2020**, 63, 244201.

[36] N. Meinzer, E. Hendry, W. L. Barnes, *Phy. Rev. B* **2013**, 88, 041407.

[37] H.-Y. Ahn, H.-E. Lee, K. Jin, K. T. Nam, *J. Mater. Chem. C* **2013**, 1.